

Polarization-sensitive broadband photodetector using a black phosphorus vertical p-n junction

Hongtao Yuan^{1,2}, Xiaoge Liu¹, Farzaneh Afshinmanesh¹, Wei Li¹, Gang Xu¹, Jie Sun¹, Biao Lian¹, Alberto G. Curto¹, Guojun Ye^{3,4}, Yasuyuki Hikita^{1,2}, Zhixun Shen^{1,2}, Shou-Cheng Zhang^{1,2}, Xianhui Chen^{3,4,5,6}, Mark Brongersma^{1,2}, Harold Y. Hwang^{1,2*} and Yi Cui^{1,2*}

The ability to detect light over a broad spectral range is central to practical optoelectronic applications and has been successfully demonstrated with photodetectors of two-dimensional layered crystals such as graphene and MoS₂. However, polarization sensitivity within such a photodetector remains elusive. Here, we demonstrate a broadband photodetector using a layered black phosphorus transistor that is polarization-sensitive over a bandwidth from ~400 nm to 3,750 nm. The polarization sensitivity is due to the strong intrinsic linear dichroism, which arises from the in-plane optical anisotropy of this material. In this transistor geometry, a perpendicular built-in electric field induced by gating can spatially separate the photogenerated electrons and holes in the channel, effectively reducing their recombination rate and thus enhancing the performance for linear dichroism photodetection. The use of anisotropic layered black phosphorus in polarization-sensitive photodetection might provide new functionalities in novel optical and optoelectronic device applications.

Confined electronic systems in layered two-dimensional crystals are host to many emerging electronic, spintronic and photonic phenomena^{1–3}, including quantum Hall and Dirac electrons in graphene^{4–6} and topological surface states in topological insulators^{7,8}. Identifying new functionalities of two-dimensional materials experimentally is a challenging and rewarding frontier, enabled by recent advances in materials and device fabrication. One example is valley polarization control using circularly polarized light in a non-centrosymmetric MoS₂ monolayer, and the resulting potential valleytronics applications^{9–11}. Other examples include recent demonstrations of novel electronic and optoelectronic applications of the well-known layered material black phosphorus (BP), such as high-mobility field-effect transistors and linear-polarization-dependent optical absorption^{12–14}. Discovering further new properties and functionalities using known layered materials is of practical importance and great current interest^{14–26}.

As a potential functionality for layered two-dimensional materials, linear dichroism is an electromagnetic spectroscopy that probes the different absorptions of light polarized parallel or perpendicular to an orientation axis. It directly depends on the conformation and orientation of material/device structures, where they are either intrinsically oriented in an anisotropic crystal structure^{27,28} or extrinsically oriented in anisotropic device patterns^{29,30}. Compared to the hexagonal in-plane lattice in other two-dimensional materials such as graphene and MoS₂, which are insensitive to the linear polarization of incident light, the layered BP crystal with its rectangular in-plane lattice has a highly anisotropic structure along the *x* and *y* directions (defined in Fig. 1a), with every two rows of P atoms alternately puckered up and down to form an ‘armchair-like’ geometry only along the *x* direction. The electrons and photons in BP can therefore behave in a highly anisotropic manner within the layer plane^{18,19}. In contrast to existing photodetectors for linear dichroism detection based on extrinsic geometric

effects (such as with wire-grid patterns^{30–33}), BP, with its mirror reflection symmetry only in the *y* direction (Supplementary Fig. 1a), offers an exciting opportunity to incorporate intrinsic crystal anisotropy for linear-polarization-sensitive photodetection. In this Article we demonstrate a linear dichroic photodetector based on BP transistors, where the polarized light is absorbed differently along two in-plane crystal axes across a very broad spectral range from ~400 nm to 3,750 nm. The optical selection rules in BP allow the broadband absorption of light polarized preferentially in the *x* direction, leading to a new degree of freedom with which to manipulate electronic and optoelectronic properties in layered BP. In particular, using the vertical p–n junction induced by an ionic gel gated transistor, we spatially separate the photogenerated electron–hole pairs in the channel, reducing their recombination rate and thus enhancing the photoresponsivity of the photodetector.

Anisotropic band structure and optical selection rules

Similar to the layered structure of other two-dimensional materials, BP is composed of stacks of its monolayer structure along the *z* axis (Fig. 1a). Unlike layered crystals with *sp*² bonding and a flat in-plane lattice, the BP monolayer, puckered along the *x* direction due to *sp*³ hybridization, creates an anisotropic band structure. We performed angle-resolved photoemission spectroscopy (ARPES) and theoretical band calculations to study the band dispersion anisotropy of BP. In the experimental band structure obtained by ARPES (Fig. 1c,d), the valence band maximum of bulk BP resides at the Z point, the centre of the *k_z* = π plane in the Brillouin zone (Fig. 1b; hereafter *k_x*, *k_y* and *k_z* represent the wavevectors along the *x*, *y* and *z* direction in momentum space, respectively)³⁴. Furthermore, the bands along the Z–L (*k_x*) and Z–P (*k_y*) directions have different evolving slopes. The elliptic pockets in the constant-energy contours (Fig. 1d) directly reflect the anisotropic effective mass and free carrier velocity along the two perpendicular

¹Geballe Laboratory for Advanced Materials, Stanford University, Stanford, California 94305, USA. ²Stanford Institute for Materials and Energy Sciences, SLAC National Accelerator Laboratory, Menlo Park, California 94025, USA. ³Hefei National Laboratory for Physical Sciences at Microscale and Department of Physics, University of Science and Technology of China, Hefei, Anhui 230026, China. ⁴Key Laboratory of Strongly-coupled Quantum Matter Physics, Chinese Academy of Sciences, Hefei, Anhui 230026, China. ⁵High Magnetic Field Laboratory, Chinese Academy of Sciences, Hefei, Anhui 230031, China. ⁶Collaborative Innovation Center of Advanced Microstructures, Nanjing University, Nanjing 210093, China. *e-mail: hyhwang@stanford.edu; yicui@stanford.edu

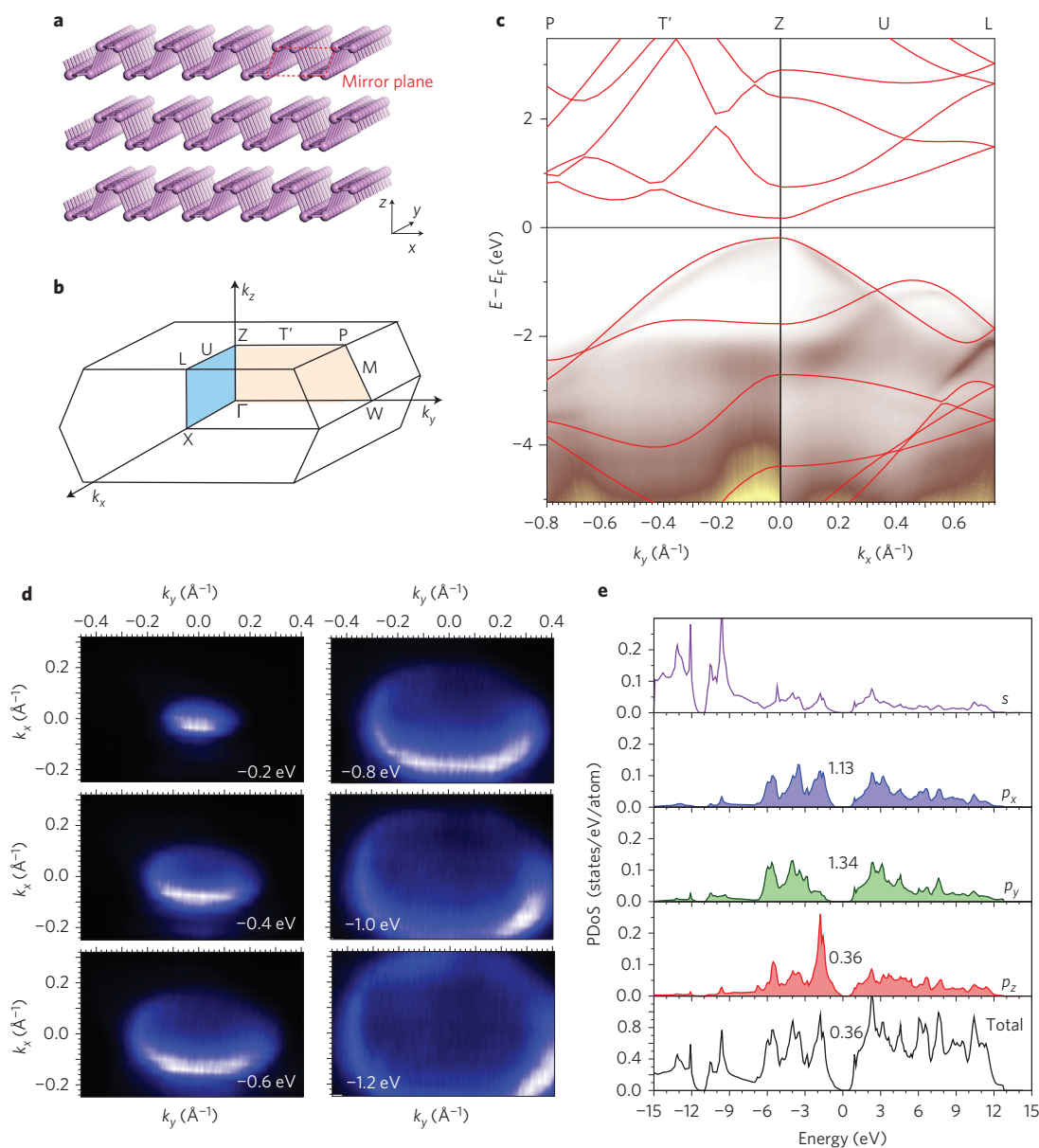


Figure 1 | Anisotropic electronic structure of layered BP. **a, b**, Layered crystal structure of BP and schematic of its three-dimensional Brillouin zone. The BP lattice shows a novel in-plane atomic buckling along the x axis, resulting in a two-fold anisotropy along the x and y directions, with a direct influence on its band structure and optical selection rules. The parallelogram plane (in red) in **a** reflects the mirror reflection symmetry in the BP structure. **c**, Band structure of cleaved bulk BP, obtained by ARPES measurements (colour mapping) and from band calculations (red lines), showing the anisotropic band dispersion and effective mass between Z-P and Z-L directions. **d**, Constant-energy contours showing the evolution of the anisotropic band dispersion at different energies from -0.2 eV to -1.2 eV. The energies shown are all with respect to the Fermi level. **e**, Partial density of states (PDoS) of BP for s , p_x , p_y , and p_z orbitals. The number in each panel indicates the gap size for each PDoS, where the p_z orbital along the z crystal axis contributes all of the band dispersion near the band edge and practically dominates the size of the bandgap of bulk BP.

in-plane directions. Band calculations indicate a direct bandgap of 0.36 eV for bulk BP, close to the experimental value (0.33 eV, discussed later). The direction with small effective masses ($0.12m_0$ for holes and $0.11m_0$ for electrons, where m_0 is the electron rest mass in vacuum) is the k_x direction (the puckering x direction in real space). In contrast, the valence (conduction) band along the k_y direction is a relatively flat band and gives a larger hole (electron) effective mass of $\sim 0.81m_0$ ($1.3m_0$), reflecting the electronic anisotropy along the Z-P and Z-L directions (Fig. 1c)¹². Considering the orbital component within this sp^3 hybridization (partial density of states shown in Fig. 1e), the band dispersions near the valence band maximum and the resulting bandgap mainly originate from the p_z orbital localized along the z direction.

A symmetry analysis from the band structure for the optical selection rules can explain why BP exhibits linear dichroism and anisotropic absorption along the two perpendicular planar directions. The BP crystal structure possesses inversion symmetry (parity) and mirror reflection symmetry (M_y) only in the y direction, as shown in Supplementary Fig. 1a. Electron states at high symmetry points (for example, Z and Γ) in the Brillouin zone can thus be labelled by these two symmetries and correspondingly there are two optical selection rules. The first is the parity selection rule, which states that, because the photons carry parity -1 , optical absorption can only occur between electron states (bands) with opposite parities. The second is the polarization selection rule, and concerns the polarization of normally incident light.

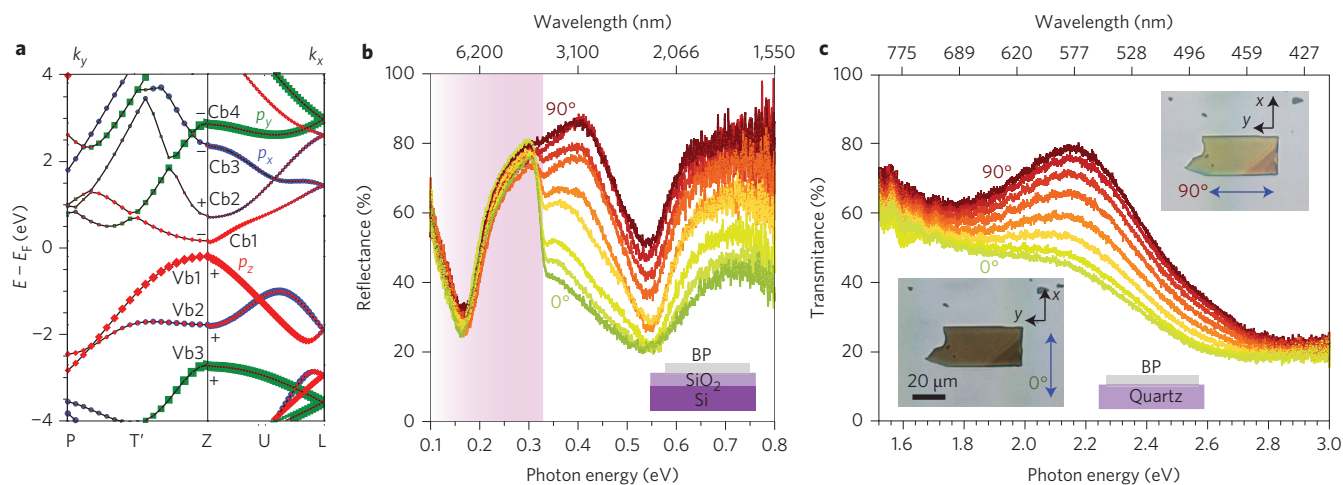


Figure 2 | Optical selection rules and broadband linear dichroism in BP. **a**, Orbital component analysis of bulk BP band dispersion. In the Z–L direction, only light polarized in the x direction can be absorbed. ‘+’ and ‘–’ represent the parity of the bands. Red, blue and green colours represent band dispersion from the p_z , p_x and p_y orbitals. **b**, Light polarization dependence of reflection in the infrared spectral regime, showing around 50% variation in reflection along two perpendicular directions for energies above the bandgap (purple shaded area). **c**, Polarization dependence of the transmission of visible light. In both **b** and **c**, the incident light is linearly polarized in directions ranging from the x to the y crystal axes (from green/ 0° to dark red/ 90°) in 15° steps. Insets in **c**: optical images with incident light along two perpendicular directions (blue arrow represents the direction of light polarization).

We denote the electric field and magnetic field of the light in x and y directions as E_x , E_y and B_x , B_y , respectively. Under mirror reflection (M_y), the electromagnetic fields of the light polarized in the y direction change sign ($E_y \rightarrow -E_y$, $B_x \rightarrow -B_x$), while those of light polarized in the x direction are unchanged ($E_x \rightarrow E_x$, $B_y \rightarrow B_y$). Accordingly, absorption of the x -direction (y -direction) polarized light is only allowed between electron states with the same (opposite) eigenvalue of M_y (for example, +1 or –1). We note that the second rule applies also for all electron states in the y -direction momentum $k_y = 0$ plane.

According to the optical selection rules, we find that the lowest-energy optical transition in BP occurs at the Z point across the gap (~ 0.33 eV) between the valence band Vb1 and the conduction band Cb1 with opposite parities (Fig. 2a)²⁷. Both bands have $M_y = +1$ at the Z point and in the $k_y = 0$ plane. The electron states in the $k_y = 0$ plane (Z–L direction in Fig. 2a) are therefore forbidden to absorb light polarized in the y direction. In contrast, states in the $k_x = 0$ plane (Z–P direction in Fig. 2a) in general have no M_y symmetry, and thus the absorption of both x - and y -direction polarized light is symmetry-allowed. Overall, the absorption of polarized light in y direction is forbidden at 0.33 eV and also significantly reduced at higher energies, which leads to the linear polarization-dependent absorption spectrum in BP. Note that the pair of bands Vb1 \leftrightarrow Cb1 can contribute to intrinsic light absorption in a broad range of photon energies from 0.33 eV to 4 eV, thus supporting a wide continuous polarization-dependent absorption spectrum. However, optical transitions between other bands will be involved for photon energies above 1.2 eV, where the polarization sensitivity is either weakened or strengthened. Based on band structure calculations (Fig. 2a) we find that all the photon absorption up to ~ 3.0 eV favour the absorption of x -polarized light, while band pairs Vb3–Cb1 and Vb1–Cb4, favouring y -polarized light, are involved in absorption processes above 3.0 eV (Fig. 2a and Supplementary Section 3). Therefore, in principle, the polarization dependence of the absorption continuously covers a wide range from 0.33 eV up to ~ 3.0 eV (3,750–400 nm in wavelength).

Linear dichroism and broadband anisotropic absorption

To experimentally verify the linear dichroism of BP, we performed polarization-dependent absorption and reflection measurements on

mechanically cleaved BP flakes (details are provided in Supplementary Section 3). In the infrared regime (Fig. 2b), the reflection spectrum with incident light polarized along the x axis of the BP crystal has a sudden drop for photon energies larger than the bandgap (0.33 eV) of BP. In contrast, the reflection of light polarized along the y axis shows no decrease near the band edge. One can clearly see the gradual evolution of the reflection spectra using light with polarization angles changing from the x to y directions. This implies that more photons are absorbed with incident light polarized along the x axis than with light polarized along the y axis, consistent with our theoretical analysis and recent optical studies^{12,18,19}. Similar polarization-dependent phenomena are observed for visible light (Fig. 2c); transmittance with light polarized along the x axis is low (42% at 2.3 eV), and the flake appears darker with more absorption (inset of Fig. 2c). By contrast, when light is polarized along the y axis, the transmittance at 2.3 eV is as high as 80% and the flake appears transparent. See Supplementary Movie, which clearly shows the gradual changes in the transmittance during continuous rotation of the polarization axis.

The polarization-dependent anisotropic absorption in BP is reflected by its photoconductivity. Scanning photocurrent microscopy was performed using a supercontinuum laser (wavelength, 400–1,700 nm) to measure the spatially dependent photoresponse of BP devices (first on a Hall bar patterned BP device, as shown in Supplementary Section 4). A small d.c. voltage ($V_{SD} = 0.1$ V) was applied between the source–drain electrodes (Supplementary Fig. 4b). As shown in a large-area photocurrent image for the whole channel (Supplementary Fig. 4c), one can see a strong signal from photocurrent $|I_{ph}|$ at two different BP–metal electrode edges and zero photoresponse in the centre area of the flake far from the electrodes. Supplementary Fig. 4d shows the evolution of photocurrent mapping images ($|I_{ph}|$) at a constant wavelength of 1,500 nm as a function of the polarization angle of the incident light, with the laser spot scanning near the metal electrode edges (indicated by the yellow square in Supplementary Fig. 4c). The photocurrent is at a maximum (showing a strip shape) when the incident light is polarized along the x crystal axis (defined as 0° polarization) and at a minimum when the incident light is polarized along the y crystal axis (defined as 90° polarization), directly indicating polarization-dependent absorption and the resulting linear dichroic photocurrent generation. Note that the photocurrent at two different BP–metal

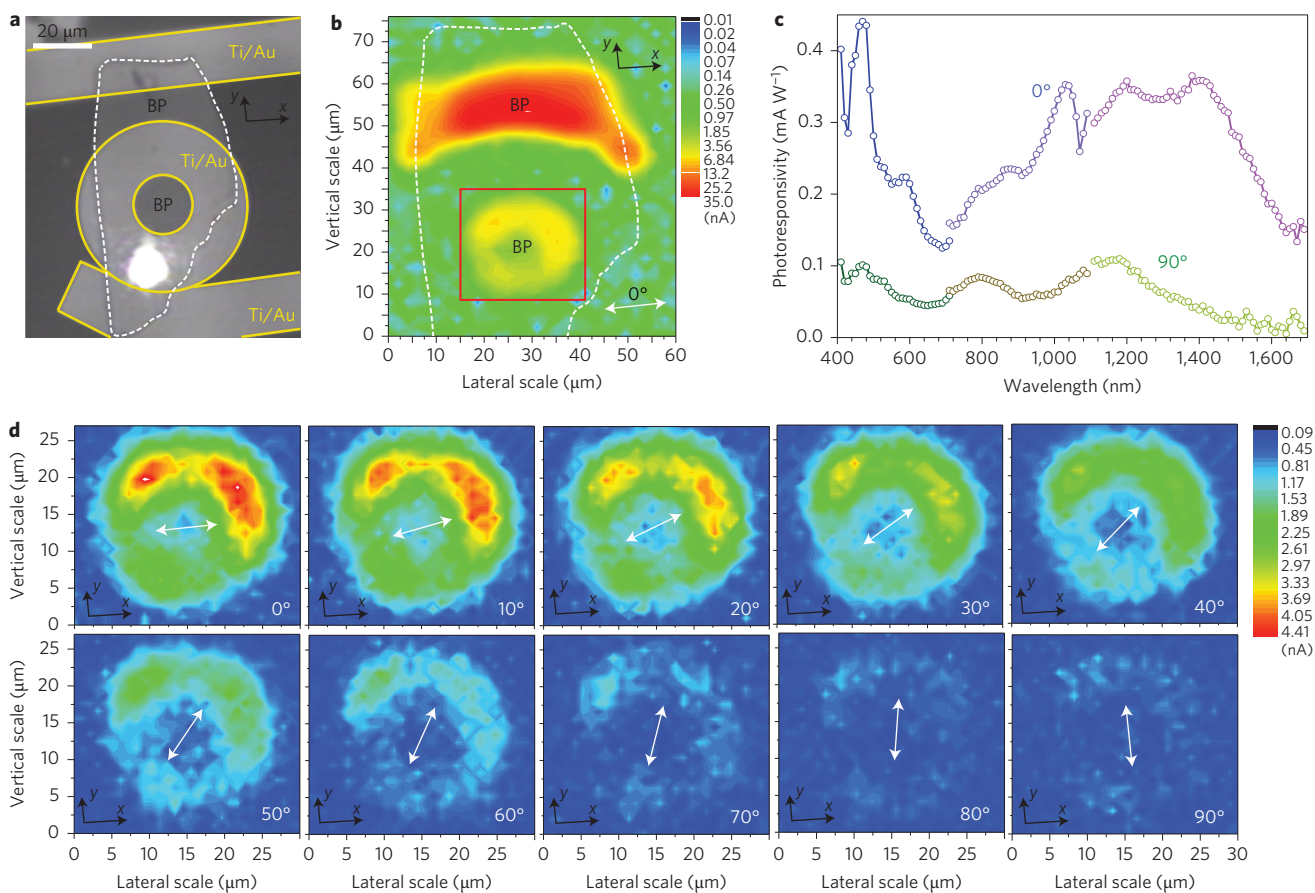


Figure 3 | BP photodetector with broadband response and polarization sensitivity. **a**, Optical image of a BP photodetector with a ring-shaped photocurrent collector. Areas indicating by yellow lines are Ti/Au electrodes and the area enclosed by a white line is the BP flake. In contrast to a straight-edge metal electrode, the isotropic round photocurrent collector can avoid the linear polarization that might arise from a straight metal edge. **b**, Corresponding photocurrent microscopy image of the device shown in **a**, with illumination at 1,500 nm and polarization along the x direction (white arrow). Further detailed investigations on the photocurrent generation focus on the BP inside the inner ring. **c**, Polarization dependence of photoresponsivity with illumination from 400 to 1,700 nm, where the polarization angle of 0° corresponds to the x crystal axis and 90° corresponds to the y crystal axis. **d**, Photocurrent microscopy images of the BP inside the inner ring under illumination at 1,500 nm with different light polarizations (white arrows). As shown in Supplementary Figs 5 and 6, similar results are observed under broadband illumination, at least within the spectral regime in our experiment (400–1,700 nm).

electrode edges has opposite directions of flow (more details are provided in Supplementary Fig. 8) and there is a zero photocurrent crossover along the channel. Such a current flow profile and the zero-photocurrent crossing along the current channel can be attributed to the photo-thermoelectric effect under pulsed excitation heating rather than a photovoltaic effect originating from the built-in electric field between the source–drain electrodes. Our systematic measurements indicate that the photo-thermoelectric effect dominates photocurrent generation at zero and low d.c. voltages ($|V_{SD}| < 0.15$ V), and the photovoltaic effect starts to dominate the photocurrent process at higher $|V_{SD}|$. More details are provided in Supplementary Section 6.

To exclude the possibility that the observed two-fold polarization-dependent photocurrent originates from a geometric edge effect at the metal–BP edge, we designed a ring-shaped metal electrode as the photocurrent collector (Fig. 3a), in which the photogenerated hot carriers can be collected isotropically and the influence from the orientation of the electrode edge is the same for all polarizations. A small d.c. voltage ($V_{SD} = 0.1$ V) was applied between the source–drain electrodes so that the device was working in the photo-thermoelectric regime, with a view to observe the intrinsic behaviour of the anisotropic BP flakes, without the photocurrent being driven by an external electric field in the photovoltaic regime. Figure 3b shows the full spatial mapping of the photocurrent

around the ring-shaped electrode at a wavelength of 1,500 nm. Focusing the excitation in the round area within the inner diameter of the electrode, the photocurrent with 0° light polarization (x crystal axis) is much larger than that for 90° light polarization (Fig. 3c), suggesting that the intrinsic polarization-dependent photo-response originates from the BP itself. The photoresponsivity (photocurrent normalized to the incident laser power) at 1,200 nm is as large as 0.35 mA W^{-1} , and there is a large contrast ratio (3.5) between the photoresponsivities along the two perpendicular polarizations.

These observations clearly indicate that the incident light in different polarization states travelling through the dichroic BP experiences a varying absorption, directly reflecting the intrinsically anisotropic orientation of the crystal structure. Related to the total intrinsic vertical optical transition for a single pair of bands ($Vb1 \leftrightarrow Cb1$ transition, as mentioned above for Fig. 2a), the photoresponsivity to polarized laser excitation with wavelength varying from 400 nm to 1,700 nm directly indicates the wide bandwidth of the linear dichroism detection (Fig. 3c). Compared to reported linear dichroism applications based on a wire-grid polarizer^{30,31}, which have largely relied on advances in nanofabrication, our photodetection observations demonstrate that layered BP can be used as a potential intrinsic linear dichroism medium with broadband response for practical integrated optical applications. Interestingly, its relatively small carrier effective masses along the

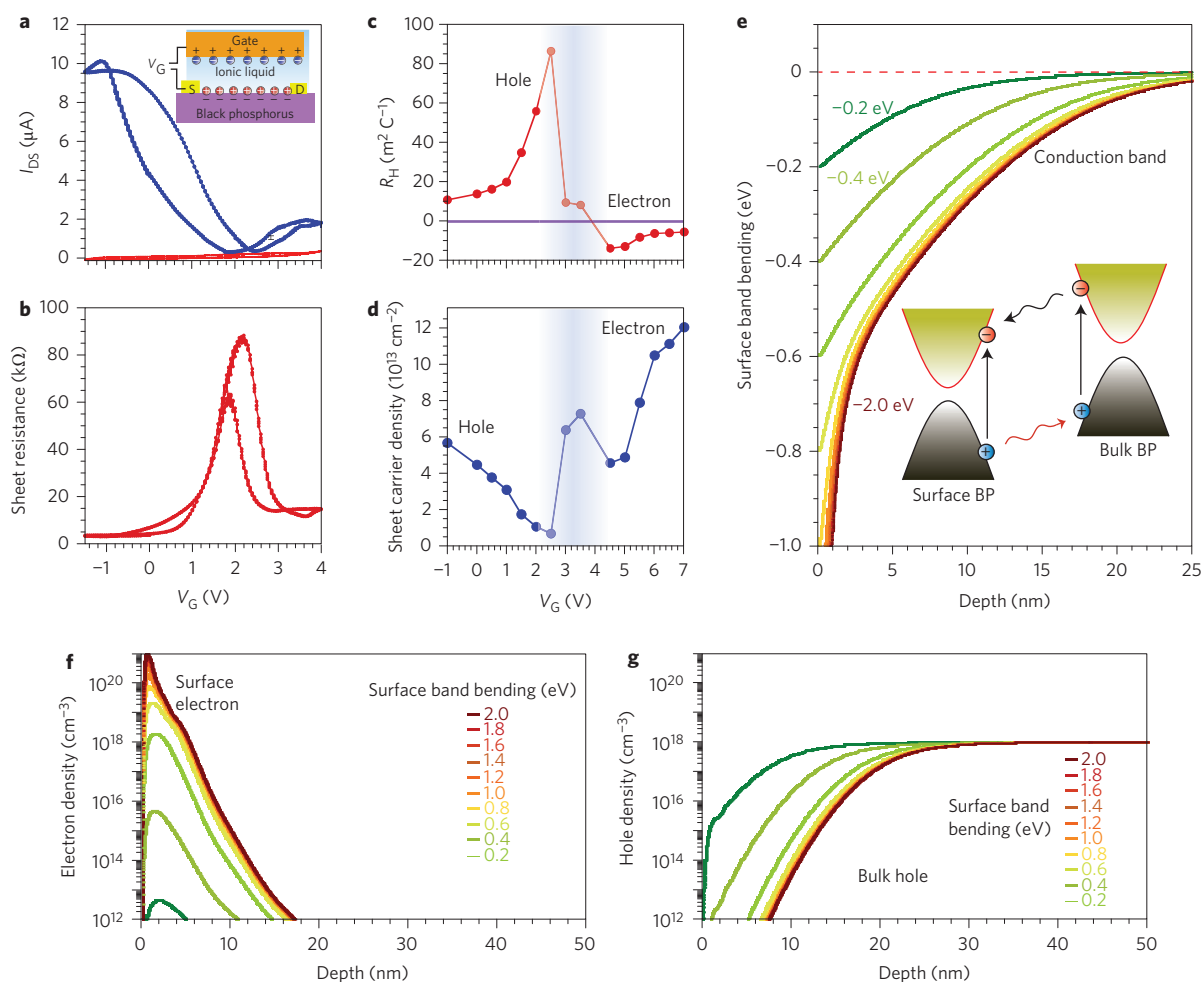


Figure 4 | Ambipolar operation and the vertical p-n junction in BP transistors. **a**, Ambipolar transfer characteristics in ionic gel gated EDLTs based on a cleaved BP flake with a thickness of ~ 30 nm. Inset: schematic structure of a typical ionic gel gated BP transistor. By applying a gate voltage V_G to the lateral Au gate electrode, ions in the gel are driven to the BP surface, forming a perpendicular electric field at the BP surface. The blue curve is the source-drain current and the red curve is the corresponding gate current, both measured at 230 K. **b**, Sheet resistance as a function of gate voltage V_G , indicating an ambipolar behaviour similar to graphene transistors. **c,d**, Hall coefficient and sheet carrier density obtained from Hall effect measurements. The maximum attainable sheet carrier densities of $0.57 \times 10^{14} \text{ cm}^{-2}$ for holes and $1.2 \times 10^{14} \text{ cm}^{-2}$ for electrons indicate the existence of surface band bending on the BP side. Shaded areas indicate the electron/hole 'puddle' regime, similar to that in graphene transistors. **e**, Self-consistent Poisson-Schrödinger calculations for surface band bending in ionic gel gated BP transistors. Green represents a weaker downward band bending (-0.2 eV) and dark red a stronger band bending (-2.0 eV). Inset: schematic diagram of the relative movement of the photogenerated carriers in the built-in electric field in a vertical p-n junction. **f,g**, Carrier distribution profile in ionic gel gated BP transistors obtained from Poisson-Schrödinger calculations for different band bending levels (as indicated by the labels), demonstrating the accumulation of electrons on the BP surface. Here, we use a bulk hole density of $1 \times 10^{18} \text{ cm}^{-3}$.

x and z directions give a carrier mobility an order of magnitude larger than for typical perovskite absorbers^{35,36} and layered chalcogenides^{16,37}. Consequently, the large carrier mobility directly affects the photoresponse speed of the BP photodetector devices. As indicated in Supplementary Section 7, the photoresponse rise time of the linear dichroic BP photodetector can be faster than $40 \mu\text{s}$, which is the time resolution limit of our photocurrent measurement set-up. This value of $40 \mu\text{s}$ is clearly faster than the photoresponse times of previously reported photodetectors based on layered chalcogenides and BP (on the order of milliseconds or slower)^{16,37}.

Photoresponsivity in a vertical p-n junction

To enhance the performance of the BP photodetector, the BP flakes were patterned into an ionic gel gated electric-double-layer transistor (EDLT), which is known to be a powerful tool to tune interfacial band bending (perpendicular electric field) and also the Fermi level of channel materials over a large range³⁸⁻⁴⁰. Figure 4a,b shows the ambipolar transfer characteristics, the source-drain current I_{DS}

and sheet resistance R_s as functions of gate voltage V_G for a BP-based EDLT. As a normally-on transistor with a p-type channel, negative V_G accumulates holes at the gel-BP interface with upward band bending. Positive V_G first depletes the holes away from the interface and, with a further increase in V_G , an electron inversion layer can be induced (Supplementary Section 8). Hall effect measurements (Fig. 4c,d) clearly indicate ambipolar operation in the channel, with the transition from hole conduction to electron conduction as V_G increases from zero to a positive value. Carriers are confined at the gel-BP interface with a maximum attainable sheet carrier density up to $1.2 \times 10^{14} \text{ cm}^{-2}$ for electrons and $0.57 \times 10^{14} \text{ cm}^{-2}$ for holes, corresponding to a Fermi level shift of ~ 0.49 eV above the conduction band minimum for electron accumulation, and ~ 0.57 eV below the valence band maximum for hole accumulation (estimated by the density of states of BP from band calculations). A qualitative estimation of the carrier distribution profile of the downward band bending case under positive V_G indicates that electrons are strongly confined at the surface, and

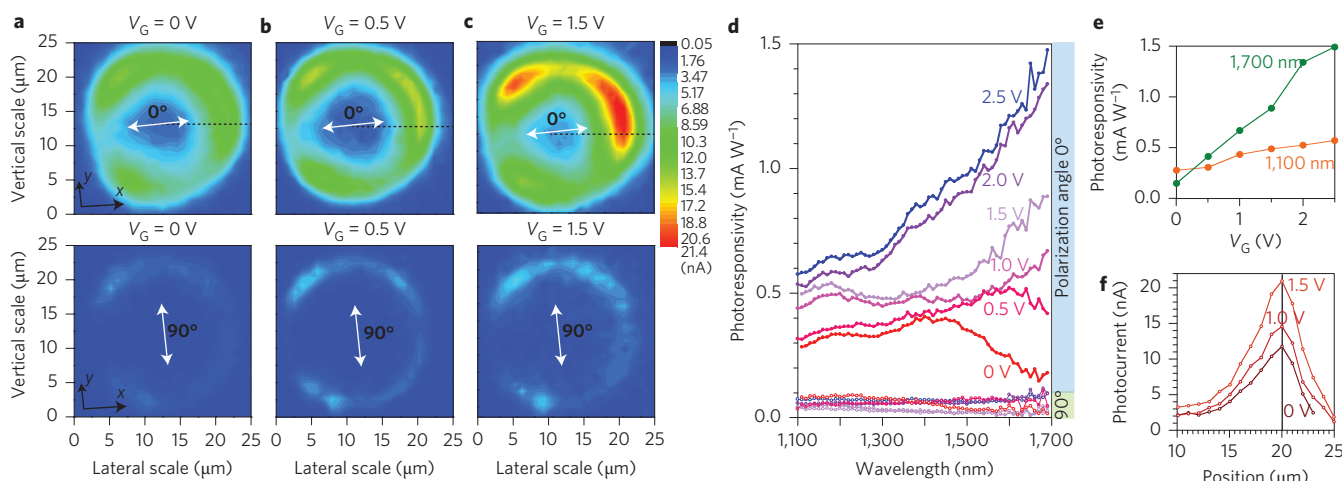


Figure 5 | Gate enhancement of linear dichroism detection by a vertical p–n junction in a BP EDLT. **a–c**, Photocurrent microscopy images of the BP device with illumination at 1,500 nm for two perpendicular polarizations under gate biases of $V_G = 0$ V (**a**), 0.5 V (**b**) and 1.5 V (**c**). A polarization angle of 0° corresponds to the x crystal axis and 90° corresponds to the y crystal axis, as indicated by white arrows. **d**, Gate-enhanced linear dichroism detection in the BP photodetector as demonstrated by the dependence of the photoresponsivity for incident light polarized along the x and y crystal axes. **e**, Gate-dependent photoresponsivity at two different wavelengths (1,100 nm and 1,700 nm) for light polarization along the x axis. **f**, Gate-dependent photocurrent profile from the centre of the ring to the metal edge along the black dashed line in **a–c** for light polarization along the x axis (1,500 nm).

holes are distributed in the deeper bulk regime (Fig. 4f,g). Interestingly, the formation of an inversion layer (surface electron accumulation) on the p-type BP channel (holes in bulk) suggests that we can easily induce a vertical p–n junction structure within such an EDLT configuration. More importantly, the depth of the depletion layer and resulting p–n junction profile can be tuned by both the external perpendicular electric field (gate voltage) and the bulk carrier density in BP crystals, providing us with freedom for rational control of the p–n junction for performance enhancement of BP photodetectors.

To this end, we varied the gate voltage V_G and obtained corresponding photocurrent images of the BP ring-shaped pattern under various V_G (Fig. 5a–c). On increasing V_G from zero bias to 1.5 V, the maximum photocurrent under illumination at 1,500 nm with 0° polarization dramatically increases and the photocurrent generation areas enlarge, while the photocurrent under light polarized at 90° does not significantly change as V_G varies. As shown in Fig. 5d,e, the photoresponsivity at 1,700 nm (0° polarization) can be enhanced by one order of magnitude by applying a positive gate voltage. Correspondingly, the ratio of the photoresponsivities between the two polarizations is greatly enhanced. The downward band bending and the resulting built-in perpendicular electric field in the BP channel in the vertical p–n junction can serve to spatially separate the photogenerated carriers (as schematically shown in the inset of Fig. 4e). Electrons move at the outmost surface while holes move in the bulk. The most direct result of this is that the recombination probability for electrons and holes during their motion to opposite electrodes can be greatly reduced^{41–44}.

To generate photocurrent, the mobile carriers move to the electrode from the light spot centre, with exponential decay due to losses such as carrier recombination:

$$n(r) = n_0 e^{-r/L_0}$$

where r is the distance from the light spot centre, L_0 is the diffusion length, and n_0 is the number of electron–hole pairs generated by the light shining on the sample with intensity I_0 . Two factors can therefore directly influence photocurrent generation: L_0 and n_0 . Experimentally, if comparing the absolute distance from the BP–metal edge (20 μm in Fig. 5f) to the position at a specific photocurrent level (10 nA), one can see that a higher V_G gives a long

distance for the lateral diffusion of hot carriers, from 1.2 μm for zero V_G , 2.2 μm for 1.0 V, to 3.7 μm for 1.5 V. However, there is almost no change in the photocurrent normalized by the maximum value at each value of V_G . This implies that the carrier diffusion length does not significantly change with V_G and is not the dominant mechanism for photocurrent enhancement. It appears, rather, that the enhancement of n_0 is key to increasing the absolute value of photocurrent. Namely, as V_G increases, the tunable perpendicular electric field can separate the electrons and holes—electrons move on the surface and holes move in the bulk, which can reduce their recombination and increase the value of n_0 .

In contrast to conventional phototransistors, photogenerated electrons and holes in our vertical p–n junction structure are separated by selectively driving them into surface or bulk layers under a built-in electric field within an EDLT. This vertical p–n junction configuration can therefore greatly enhance the efficiency of the linear dichroism photodetector. Although far from optimized, our observations provide the first demonstration that a vertical p–n junction device structure can have a significant role in performance enhancement in a linear dichroism photodetection scheme using BP. Key to this approach is a direct combination of the intrinsic broadband linear dichroism of BP and its high-mobility semiconductor characteristics, which can enable novel integrated optical and optoelectronic device applications beyond conventional materials and approaches.

Methods

Methods and any associated references are available in the [online version of the paper](#).

Received 16 September 2014; accepted 27 April 2015; published online 1 June 2015

References

- Geim, A. K. & Grigorieva, I. V. Van der Waals heterostructures. *Nature* **499**, 419–425 (2013).
- Wang, Q. H., Kalantar-Zadeh, K., Kis, A., Coleman, J. N. & Strano, M. S. Electronics and optoelectronics of two-dimensional transition metal dichalcogenides. *Nature Nanotech.* **7**, 699–712 (2012).
- Novoselov, K. S. *et al.* Two-dimensional gas of massless Dirac fermions in graphene. *Nature* **438**, 197–200 (2005).

4. Zhang, Y. B., Tan, Y. W., Stormer, H. L. & Kim, P. Experimental observation of the quantum Hall effect and Berry's phase in graphene. *Nature* **438**, 201–204 (2005).
5. Novoselov, K. S. *et al.* Room-temperature quantum Hall effect in graphene. *Science* **315**, 1379–1379 (2007).
6. Bolotin, K. I., Ghahari, F., Shulman, M. D., Stormer, H. L. & Kim, P. Observation of the fractional quantum Hall effect in graphene. *Nature* **462**, 196–199 (2009).
7. Chen, Y. L. *et al.* Experimental realization of a three-dimensional topological insulator, Bi₂Te₃. *Science* **325**, 178–181 (2009).
8. Zhang, H. J. *et al.* Topological insulators in Bi₂Se₃, Bi₂Te₃ and Sb₂Te₃ with a single Dirac cone on the surface. *Nature Phys.* **5**, 438–442 (2009).
9. Mak, K. F., He, K. L., Shan, J. & Heinz, T. F. Control of valley polarization in monolayer MoS₂ by optical helicity. *Nature Nanotech.* **7**, 494–498 (2012).
10. Zeng, H. L., Dai, J. F., Yao, W., Xiao, D. & Cui, X. D. Valley polarization in MoS₂ monolayers by optical pumping. *Nature Nanotech.* **7**, 490–493 (2012).
11. Cao, T. *et al.* Valley-selective circular dichroism of monolayer molybdenum disulphide. *Nature Commun.* **3**, 887 (2012).
12. Li, L. K. *et al.* Black phosphorus field-effect transistors. *Nature Nanotech.* **9**, 372–377 (2014).
13. Liu, H. *et al.* Phosphorene: an unexplored 2D semiconductor with a high hole mobility. *ACS Nano* **8**, 4033–4041 (2014).
14. Low, T. *et al.* Tunable optical properties of multilayers black phosphorus thin films. *Phys. Rev. B* **90**, 075434 (2014).
15. Xu, Y. *et al.* Large-gap quantum spin Hall insulators in tin films. *Phys. Rev. Lett.* **111**, 136804 (2013).
16. Buscema, M. *et al.* Fast and broadband photoresponse of few-layer black phosphorus field-effect transistors. *Nano Lett.* **14**, 3347–3352 (2014).
17. Lopez-Sanchez, O., Lembke, D., Kayci, M., Radenovic, A. & Kis, A. Ultrasensitive photodetectors based on monolayer MoS₂. *Nature Nanotech.* **8**, 497–501 (2013).
18. Xia, F., Wang, H. & Jia, Y. Rediscovering black phosphorus as an anisotropic layered material for optoelectronics and electronics. *Nature Commun.* **5**, 4458 (2014).
19. Qiao, J., Kong, X., Hu, Z. X., Yang, F. & Ji, W. High-mobility transport anisotropy and linear dichroism in few-layer black phosphorus. *Nature Commun.* **5**, 4475 (2014).
20. Low, T. *et al.* Plasmons and screening in monolayer and multilayer black phosphorus. *Phys. Rev. Lett.* **113**, 106802 (2014).
21. Low, T., Engel, M., Steiner, M. & Avouris, P. Origin of photoresponse in black phosphorus photo-transistors. *Phys. Rev. B* **90**, 081408 (2014).
22. Fei, R. *et al.* Enhanced thermoelectric efficiency via orthogonal electrical and thermal conductances in phosphorene. *Nano Lett.* **14**, 6393–6399 (2014).
23. Engel, M., Steiner, M. & Avouris, P. A black phosphorus photo-detector for multispectral, high-resolution imaging. *Nano Lett.* **14**, 6414–6417 (2014).
24. Buscema, M., Groenendijk, D. J., Steele, G. A., van der Zant, H. S. J. & Castellanos-Gomez, A. Photovoltaic effect in few-layer black phosphorus PN junctions defined by local electrostatic gating. *Nature Commun.* **5**, 4651 (2014).
25. Deng, Y. *et al.* Black phosphorus-monolayer MoS₂ van der Waals heterojunction p–n diode. *ACS Nano* **8**, 8292–8299 (2014).
26. Kamalakar, M. V., Madhushankar, B. N., Dankert, A. & Dash, S. P. Low Schottky barrier black phosphorus field-effect devices with ferromagnetic tunnel contacts. *Small* <http://dx.doi.org/10.1002/smll.201402900> (2015).
27. Dresselhaus, G. Optical absorption band edge in anisotropic crystals. *Phys. Rev.* **105**, 135–138 (1957).
28. Blakemore, J. S. & Nomura, K. C. Intrinsic optical absorption in tellurium. *Phys. Rev.* **127**, 1024–1029 (1962).
29. Wang, J. F., Gudiksen, M. S., Duan, X. F., Cui, Y. & Lieber, C. M. Highly polarized photoluminescence and photodetection from single indium phosphide nanowires. *Science* **293**, 1455–1457 (2001).
30. Nanot, S. *et al.* Broadband, polarization-sensitive photodetector based on optically-thick films of macroscopically long, dense, and aligned carbon nanotubes. *Sci. Rep.* **3**, 1335 (2013).
31. Liao, Y. L. & Zhao, Y. Design of wire-grid polarizer with effective medium theory. *Opt. Quantum Electron.* **46**, 641–647 (2014).
32. Miyamaru, F. & Hangyo, M. Polarization response of two-dimensional metallic photonic crystals studied by terahertz time-domain spectroscopy. *Appl. Opt.* **43**, 1412–1415 (2004).
33. Guillaume, M. *et al.* Polarization sensitive silicon photodiodes using nanostructured metallic grids. *Appl. Phys. Lett.* **94**, 193503 (2009).
34. Han, C. Q. *et al.* Electronic structures of black phosphorus studied by angle-resolved photoemission spectroscopy. *Phys. Rev. B* **90**, 085101 (2014).
35. Lee, M. M., Teuscher, J., Miyasaka, T., Murakami, T. N. & Snaith, H. J. Efficient hybrid solar cells based on meso-superstructured organometal halide perovskites. *Science* **338**, 643–647 (2012).
36. Stranks, S. D. *et al.* Electron-hole diffusion lengths exceeding 1 micrometer in an organometal trihalide perovskite absorber. *Science* **342**, 341–344 (2013).
37. Jacobs-Gedrim, R. B. *et al.* Extraordinary photoresponse in two-dimensional In₂Se₃ nanosheets. *ACS Nano* **8**, 514–521 (2014).
38. Cho, J. H. *et al.* Printable ion-gel gate dielectrics for low-voltage polymer thin-film transistors on plastic. *Nature Mater.* **7**, 900–906 (2008).
39. Kawasaki, M. & Iwasa, Y. Electronics: 'cut and stick' ion gels. *Nature* **489**, 510–511 (2012).
40. Yuan, H. T. *et al.* Zeeman-type spin splitting controlled by an electric field. *Nature Phys.* **9**, 563–569 (2013).
41. Yu, W. J. *et al.* Highly efficient gate-tunable photocurrent generation in vertical heterostructures of layered materials. *Nature Nanotech.* **8**, 952–958 (2013).
42. Kim, C. O. *et al.* High photoresponsivity in an all-graphene p–n vertical junction photodetector. *Nature Commun.* **5**, 3249 (2014).
43. Liu, C. H., Chang, Y. C., Norris, T. B. & Zhong, Z. H. Graphene photodetectors with ultra-broadband and high responsivity at room temperature. *Nature Nanotech.* **9**, 273–278 (2014).
44. Hu, L., Dalgleish, S., Matsushita, M. M., Yoshikawa, H. & Awaga, K. Storage of an electric field for photocurrent generation in ferroelectric-functionalized organic devices. *Nature Commun.* **5**, 3279 (2014).
45. Kresse, G. & Hafner, J. *Ab initio* molecular-dynamics for liquid-metals. *Phys. Rev. B* **47**, 558–561 (1993).
46. Kresse, G. & Joubert, D. From ultrasoft pseudopotentials to the projector augmented-wave method. *Phys. Rev. B* **59**, 1758–1775 (1999).
47. Perdew, J. P., Burke, K. & Ernzerhof, M. Generalized gradient approximation made simple. *Phys. Rev. Lett.* **77**, 3865–3868 (1996).
48. Hohenberg, P. & Kohn, W. Inhomogeneous electron gas. *Phys. Rev. B* **136**, B864 (1964).

Acknowledgements

This work was supported by the Department of Energy, Office of Basic Energy Sciences, Division of Materials Sciences and Engineering (contract no. DE-AC02-76SF00515). X.L., F.A., A.G.C. and M.L.B. acknowledge support from the Department of Energy (grant no. DE-FG07-ER46426). A.G.C. acknowledges the support of a Marie Curie International Outgoing Fellowship. G.J.Y. and X.H.C. acknowledge the support from Strategic Priority Research Program (B) of the Chinese Academy of Sciences and the National Basic Research Program of China (973 Program).

Author contributions

H.T.Y., H.Y.H. and Y.C. conceived and designed the experiments. H.T.Y. performed sample fabrication and transport measurements. H.T.Y., X.G.L., F.A., A.G.C. and M.B. performed optical measurements. W.L. and Z.X.S. performed ARPES measurement. G.X., B.L. and S.C.Z. performed DFT calculations and theoretical analyses. X.G.L. performed the band bending calculation. J.S. performed transmission electron microscopy analysis. G.J.Y. and X.H.C. grew the high-quality BP crystals. Y.H., M.B., Z.X.S., S.C.Z., X.H.C., H.Y.H. and Y.C. supervised the project and all authors contributed to data discussions. H.T.Y. wrote the manuscript, with input from all authors.

Additional information

Supplementary information is available in the [online version](#) of the paper. Reprints and permissions information is available online at www.nature.com/reprints. Correspondence and requests for materials should be addressed to H.Y.H. and Y.C.

Competing financial interests

The authors declare no competing financial interests.

Methods

Device fabrication of BP photodetector. Hall bar patterns and ring-shaped patterns with Ti/Au electrodes were fabricated on tape-cleaved BP single crystal flakes (on SiO₂/Si wafer), which typically have dimensions of tens of micrometres laterally and a thickness of 30–50 nm. The bulk BP crystal shows the p-type conduction with carrier density on the order of 10¹⁸ cm⁻³. The ring-shaped pattern is designed to exclude the possibility that the observed polarization-dependent absorption might originate from anisotropic scattering from the BP–metal edge. Serving as the side gate electrode for gel gated transistors, a large-area Ti/Au pad was deposited near the BP, but electrically insulated from the BP flake. A typical EDLT was fabricated by spin-coating DEME-TFSI-based ionic gel³⁵ (DEME-TFSI, *N,N*-diethyl-*N*-(2-methoxyethyl)-*N*-methylammonium bis-trifluoromethylsulfonyl)-imide, Kanto Chemical Co.). Note that the ionic gel is transparent within the spectral regime from 300 nm to 3,100 nm, covering the optical measurement regime (400–1,700 nm). Transfer characteristics, longitudinal sheet resistance R_s and the Hall coefficient of Hall bar patterned devices were simultaneously measured in a liquid-helium cryostat with a 14 T superconducting magnet.

Optical measurements and scanning photocurrent microscopy. Optical reflectance and transmittance spectral measurements were carried out under ambient conditions at room temperature for samples on transparent quartz substrates. The spectra in the visible regime (1.5–3.0 eV) were obtained with a confocal scanning microscope (Nikon LV-UDM with C1 confocal head) equipped with a halogen lamp, a grating spectrometer and a charge-coupled device camera. The detection area had a spot diameter of 10 μm . For reflection measurements in the infrared, we used a Nicolet 6700 Fourier-transform infrared spectrometer equipped with a Continuum XL microscope (Thermo Electron Corp.). An infrared light source was focused by a $\times 15$ Cassegrain objective with angles ranging from 16 to 35.5° with respect to the sample normal. A variable knife-edge aperture located

within the image plane was used to define the sample collection area, which was fixed in size to $\sim 200 \mu\text{m} \times 200 \mu\text{m}$. The spectral range was 650–6,500 cm⁻¹ (~ 0.08 –0.8 eV) with a resolution of 4 cm⁻¹. All spectra are the average of 32 scans. The reflectance spectra were plotted as $(R_{\text{sample}}/R_{\text{Au}}) \times 100\%$; R_{sample} was collected from an area with a sample present and R_{Au} from an adjacent Au pad as a total reflection mirror.

In photocurrent measurements, optical radiation of a well-defined wavelength was selected from a supercontinuum white-light laser source using acousto-optic tunable filters (Fianium). The laser beam passed through a linear polarizer and a half-wave plate and was then focused on the detector using a microscope objective (Mitutoyo $\times 50$, 0.42 NA). The laser beam was modulated with a mechanical chopper (1 kHz) and the modulated photocurrent signal amplified and detected using a lock-in technique. The photodetector device was mounted on a piezoelectric stage and a photocurrent image of the detector was obtained by raster-scanning the laser beam over it. To investigate the time response of the detector, we illuminate it instead with an electrically modulated diode laser at 780 nm (Toptica DL-100), driven by a square-wave function generator. After passing through a preamplifier, the photodetector signal was recorded in time by a digital oscilloscope.

ARPES and *ab initio* band calculations. High-resolution ARPES experiments for cleaved BP samples were performed at the Synchrotron Radiation Light Source Beamline 5–4 under a base pressure better than 3×10^{-11} torr, using incident photon energies of 19.5 eV with an energy resolution of 12.5 meV and angular resolution of 0.2°. Electronic structure calculations were carried out using the Vienna Ab-initio Simulation Package (VASP)^{45,46} based on experimental lattice constants and optimized internal parameters with accuracy smaller than 0.01 eV \AA^{-1} . The Perdew–Burke–Ernzerhof-type generalized gradient approximation^{47,48} with MBJ correction was used to obtain an accurate semiconducting gap. The k -mesh for self-consistent calculations was $12 \times 12 \times 16$ and the cutoff energy was fixed at 400 eV.